

Magneto-structural coupling in ilmenite-type NiTiO_3 : a combined diffraction and dilatometry study

K. Dey,^{1,*} S. Sauerland,¹ B. Ouladdiaf,² K. Beauvois,² H. Wadepohl,³ and R. Klingeler^{1,4}

¹*Kirchhoff Institute of Physics, Heidelberg University, INF 227, 69120, Heidelberg, Germany*

²*Institut Laue-Langevin, CS20156, 38042 GRENOBLE Cedex 9 - France*

³*Institute of Inorganic chemistry, Heidelberg University, 69120, Heidelberg, Germany*

⁴*Center for Advance Materials (CAM), Heidelberg University, INF 227, D-69120, Heidelberg, Germany*

(Dated: February 19, 2021)

We report the ground state magnetic structure and in-field magnetostrictive effects of NiTiO_3 studied by means of zero field and in-field single crystal neutron diffraction, magnetization and high-resolution dilatometry experiments. Zero-field neutron diffraction on NiTiO_3 single crystals reveal an easy-plane antiferromagnet with a multidomain ground state. Upon application of external magnetic fields, neutron diffraction shows the evolution of domains with spins perpendicular to the applied field. The rotation of spins in the multidomain state exhibits pronounced lattice changes in the magnetostriction measurements. We see magnetization and magnetostriction measurements sale with each other in the multidomain state revealing the strong coupling of spins to the lattice.

PACS numbers:

I. INTRODUCTION

Layered honeycomb magnets have been a great avenue for exciting and rich physics since time immemorial. The recent theoretical and experimental studies into Kitaev quantum spin-liquid in Co-based honeycomb materials^{1,2}, Dirac magnons³ and topological spin excitations⁴ in honeycomb ferromagnets, non-reciprocal magnons in honeycomb antiferromagnets⁵, zig-zag⁶ and incommensurate^{7,8} spin ground states or 2D magnetism in Van-der-Waals materials⁹ have resulted in enormous interest in these class of materials. Moreover, the spin-lattice coupling in several honeycomb magnets such as $\text{Fe}_4\text{Nb}_2\text{O}_9$ ¹⁰, $\text{Na}_3\text{Ni}_2\text{SbO}_6$ ¹¹, and $\text{Co}_4\text{Nb}_2\text{O}_9$ ¹² have resulted in significant magnetoelectric coupling and hence motivating possible technological applications.

Ilmenite titanates with chemical formula $M\text{TiO}_3$ ($M = \text{Mn}, \text{Fe}, \text{Co}, \text{Ni}$) form an isostructural series of antiferromagnetic (AFM) compounds where magnetic M^{2+} ions in the basal ab -plane exhibit a buckled honeycomb-like structure. The M^{2+} ions are interconnected via oxygen ions (O^{2-}) leading to $M\text{-O-M}$ as the dominant superexchange pathway¹³. Along c axis the crystal structure exhibits alternating layers of corner sharing TiO_6 and MO_6 octahedra resulting in relatively weaker $M\text{-O-Ti-O-M}$ superexchange pathways. Depending on the single ion-anisotropies of the respective metal ions, various magnetic ground states are realised in ilmenites, for example uniaxial AFM ground state with spins pointing along c -axis in MnTiO_3 ¹⁴ whereas an easy-plane type AFM with spins lying in the ab -plane for NiTiO_3 and CoTiO_3 ¹⁵ respectively.

Although, these compounds have been rigorously investigated since 1950s^{13,14,16-18}, recent studies evidencing linear magnetoelectric coupling in MnTiO_3 ¹⁹, large spontaneous magnetostriction in FeTiO_3 ²⁰, magnetodielectric and magnetoelastic coupling in NiTiO_3 ^{21,22} and CoTiO_3 ²³, respectively, as well as the observance of Dirac magnons in CoTiO_3 ^{24,25} have peaked enormous interest in these class of materials.

The least investigated compound among the ilmenites family, i.e., NiTiO_3 , develops long-range AFM order at

$T_N = 22.5 \text{ K}$ ^{16,21,22,26}. Recent studies of the dielectric permittivity and the thermal expansion show a pronounced magnetodielectric effect²¹ as well as distinct significant magnetoelastic coupling²². Notably, at T_N , there is single energy scale dominantly driving the observed structural, magnetic and dielectric anomalies²². In this report, we study in detail the magneto-structural coupling of NiTiO_3 by means of single crystal X-ray and neutron diffraction and high-resolution neutron dilatometry. We observe by means of single-crystal neutron diffraction that the macroscopic structural symmetry($R\bar{3}$) is retained down to the lowest measured temperature of 2 K within the experimental resolution. In addition, the magnetic ground state of NiTiO_3 is solved. At T_N , in addition to long-range AFM order, a significant lattice distortion evolves revealing large spontaneous magnetostriction in NiTiO_3 . In applied magnetic fields, the multi-domain ground state evolves to a spin-reoriented single domain state characterized by spins aligned perpendicular to the applied magnetic field. Magnetostriction measurements in the low-field region show pronounced effects due to magnetoelastic domains and remarkably scales with magnetization measurements confirming both significant magneto-structural coupling and the magneto-structural domain model in NiTiO_3 .

II. EXPERIMENTAL METHODS

Macroscopic single crystals of NiTiO_3 have been grown by means of the optical floating-zone technique in a four mirror optical floating-zone furnace (CSC, Japan) equipped with $4 \times 150 \text{ W}$ halogen lamps. Details of the growth process and characterization the single crystals have been published previously²². Single crystal X-ray intensity data were obtained at 100 K with an Agilent Technologies Supernova-E CCD 4-circle diffractometer (Mo- $\text{K}\alpha$ radiation $\lambda=0.71073 \text{ \AA}$, micro-focus X-ray tube, multilayer mirror optics). Static magnetisation $\chi = M/B$ was studied in magnetic fields up to 5 T in a Quantum Design MPMS-XL5 SQUID magnetometer. The relative length changes dL_i/L_i were studied on a

cuboid-shaped single crystal of dimensions $2 \times 1.85 \times 1 \text{ mm}^3$ by means of a three-terminal high-resolution capacitance dilatometer^{11,27}. Magnetostriction, i.e., field-induced length changes $dL_i(B)/L_i$, was measured at several fixed temperatures in magnetic fields up to 15 T and the longitudinal magnetostriction coefficient $\lambda_i = 1/L_i \cdot dL_i(B)/dB$ was derived. The magnetic field was applied along the direction of the measured length changes.

Single crystal neutron diffraction experiments were performed up to 6 T magnetic fields on the D10 beamline of the Institut Laue-Langevin (ILL) at Grenoble, France. To determine the magnetic ground state at $B = 0$ T, the four-circle configuration was used with a $96 \times 96 \text{ mm}^2$ two-dimensional microstrip detector. An incident wavelength of 2.36 Å using a vertically focusing pyrolytic graphite (PG)(002) monochromator was employed. A pyrolytic graphite filter was used in order to suppress higher-order contamination to 10^{-4} times that of the primary beam intensity. Measurements were made in the temperature range 2-50 K. The magnetic field-driven evolution of the magnetic structure at $T = 2$ K was studied by mounting the sample in a 6 T vertical cryomagnet and aligned to within 1° of magnetic field. The magnetic field was applied along the b -axis limiting the scattering to the $(H, 0, L)$ plane.

III. EXPERIMENTAL RESULTS

A. Single-crystal X-ray Diffraction

To the best of our knowledge, the earlier studies of the ilmenite-type NiTiO_3 crystal structure have been limited to powder diffraction experiments only^{14,22,28}. We have re-investigated the crystal structure by means of single-crystal high resolution XRD at 100 K, using Mo $K\alpha$ radiation ($\lambda = 0.71073$ Å). A single crystal splinter of size $0.16 \times 0.14 \times 0.01 \text{ mm}^3$ was broken off from larger specimen and used for data collection. A full shell of intensity data was collected up to 0.4 Å resolution (24180 reflections, 1028 independent [$R_{int} = 0.05$] of which 1024 were observed [$I > 2\sigma(I)$]). Detector frames (typically ω , occasionally ϕ -scans, scan width 0.5°) were integrated by profile fitting²⁹. Data were corrected for air and detector absorption, Lorentz and polarization effects³⁰ and scaled essentially by application of appropriate spherical harmonic functions³⁰⁻³². Absorption by the crystal was treated numerically (Gaussian grid)^{32,33}. An illumination correction was performed as part of the numerical absorption correction³². Space group $R-3$ was assigned based on systematic absences and intensity statistics (refined over centered unit cell on hexagonal axes, Hall group $-R3$, $a = 5.02762(6)$, $c = 13.76711(17)$ Å, $V = 301.369(8)$ Å³, $Z = 6$). This choice was confirmed by analysis of the symmetry of the phases obtained ab initio in P1. The structure was solved by intrinsic phasing³⁴⁻³⁶ and refined by full-matrix least-squares methods based on F^2 against all unique reflections³⁷⁻⁴⁰. Three somewhat different models were employed for the atomic structure factors f_{at} within the ISA approximation: conventional f_{at} calculated with neutral atoms⁴¹ for Ni, Ti and O (model A) and two

“ionic” models⁴¹ (f_{at} for Ni^{2+} , Ti^{4+} taken from ref.41 and O^{2-} from ref.42 (model B) or ref.43, respectively (model C)). An empirical secondary extinction correction^{38,44} was applied in each case but proved insignificant. The different models refined to essentially the same structure, with only insignificant differences in key parameters like atom coordinates, R factors, U_{eq} for all atoms and residual electron density. Ni-O and Ti-O bond lengths agreed within one standard deviation. There was no evidence of cation mixing and fully occupied sites were employed for all atoms. The results confirm the assignment of the space group and improve on the accuracy of the crystallographic parameters previously obtained from powder XRD and neutron data^{14,22,28}. Fractional atomic coordinates, Wyckoff positions, site occupation and equivalent isotropic displacement parameters for model A are listed in table I⁴⁵.

TABLE I: Fractional atomic coordinates, Wyckoff positions, site occupation and equivalent isotropic displacement parameters (Å²) for NiTiO_3 at 100 K as obtained from refinement of model A. (Note: (1) These co-ordinates are correct but do not form uniquely bonded set; (2) ^a U_{eq} is defined as one third of the trace of the orthogonalized U_{ij} tensor. The anisotropic displacement factor exponent takes the form: $-2\pi^2[h^2a^{*2}U_{11} + \dots + 2hka^*b^*U_{12}]$.)

Atom	Site	x	y	z	sof	U_{eq}^a
Ni	6c	0	0	0.35051(2)	1	0.00308(2)
Ti	6c	0	0	0.14422(2)	1	0.00297(3)
O	18f	0.35198(8)	0.03455(8)	0.08662(2)	1	0.00421(4)

B. Single-crystal neutron diffraction

The crystal structure at lower temperatures and the magnetic ground state of NiTiO_3 were determined by means of single-crystal neutron diffraction. At 50 K, 110 nuclear Bragg reflections were collected. Appropriate correction for extinction, absorption, and Lorentz factor was applied to all the nuclear Bragg peaks. All the nuclear peaks at 50 K were successfully indexed in the $R-3$ space group with lattice parameters $a = 5.03$ Å and $c = 13.789$ Å.

In order to clarify the magnetic structure, preliminary reciprocal-space scans (not shown here) were performed at 2 K along the $(0, 0, L)$, $(H, 0, 0)$, and $(H, K, 0)$ directions. The scans reveal a peak of significant intensity emerging at $(0,0,1.5)$, indicative of the propagation vector $\mathbf{k} = (0,0,1.5)$. In order to determine the detailed magnetic structure, integrated intensities of 187 nuclear reflections allowed within the space group $R-3$ and 292 satellite magnetic reflections were collected at 2 K. The nuclear structure was firstly refined using FULLPROF program within the $R-3$ space group. The results of refinement are listed in table II and the observed and calculated intensities from the Rietveld fits are shown in Fig. 2(a). No peak splitting or significant broadening was observed within the experimental resolution in respective 2 K nuclear reflections as compared to 50 K, indicating that the macroscopic $R-3$ symmetry is maintained until the lowest

measured temperatures. The nuclear Bragg peaks show no temperature dependence between 2 K and 50 K excluding $\mathbf{k} = (0,0,0)$.

TABLE II: Parameters for the nuclear structure of NiTiO₃ measured at 2 K obtained from refinements of single-crystal neutron diffraction data. The isotropic temperature factors (B) of all atoms were refined. [Space group: $R\bar{3}$ (148); Lattice parameters: $a = b = 5.0229(1)$ Å, $c = 13.7720(1)$ Å, $\alpha = \beta = 90^\circ$, $\gamma = 120^\circ$.

Atom	Site	x	y	z	$B_{iso}(\text{Å}^2)$
Ni1	6c	0	0	0.3537(2)	0.00748
Ti1	6c	0	0	0.1338(5)	0.06643
O1	18f	0.3344(6)	0.0052(1)	0.2466(2)	0.09830

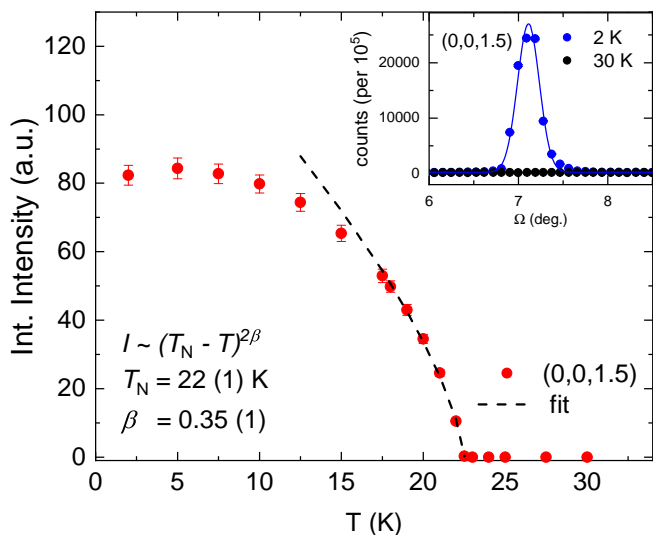


FIG. 1: Temperature dependence of the integrated intensity of the $(0,0,1.5)$ magnetic Bragg peak. The dashed black curve is a fit to the data with the power law $I \sim (T_N - T)^{2\beta}$. The inset shows the Ω scan through the magnetic $(0,0,1.5)$ peak at 2 K and 30 K respectively. The solid blue line is the Gaussian fit to the peak at 2 K. See the text for more details.

All the finite intensity magnetic peaks are observed at the general position $(H, K, L) + (0,0,1.5)$ with H, K, L satisfying the reflection conditions of the $R\bar{3}$ space group and hence confirming $\mathbf{k} = (0,0,1.5)$. A few of the observed high-intensity magnetic peaks are listed in Table III. The largest diffraction intensity occurs for the magnetic Bragg peak $(0,0,1.5)$ indicating that the Ni²⁺-moments lie in the ab plane which had been suggested by previous magnetization measurements²². The temperature dependence of the integrated intensity of the commensurate reflection $(0,0,1.5)$ in Fig. 1 shows finite intensity below the magnetic ordering temperature. A power law fit in the critical region using $I \propto M^2 \propto \tau^{2\beta}$ where M is the order parameter and $\tau = 1 - T/T_N$ results in $T_N = 22(1)$ K and $\beta = 0.35(1)$. The obtained value T_N from the power law fit agrees to the one from previous macroscopic studies^{16,21,22,26}. The obtained critical parameter indicates that Ni²⁺-spins in NiTiO₃ are of 3D Heisenberg nature.

TABLE III: Observed intensities (I_{obs}) of several high-intensity magnetic peaks as measured in D10 at 2 K and their corresponding calculated intensities (I_{cal}) as discussed in the text.

Q	I_{obs}	I_{cal}
(0,2,2.5)	975(17)	917
(0,2,5.5)	1410(27)	1307
(0,-1,5.5)	2481(36)	2685
(0,0,4.5)	2809(22)	3348
(1,-2,-1.5)	1923(20)	2045
(1,-2,4.5)	1755(22)	1521
(0,-1,2.5)	1787(17)	1965
(-1,2,4.5)	1812(48)	1521
(0,-1,8.5)	1729(109)	1679
(0,0,1.5)	4366(21)	3942

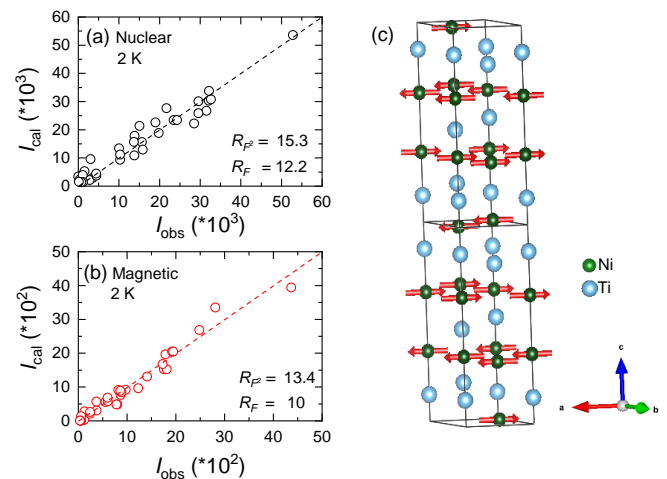


FIG. 2: Comparison between the observed and calculated integrated intensities of the non-equivalent nuclear (a) and magnetic (b) reflections, respectively, at 2 K, and (c) easy-plane type magnetic structure of NiTiO₃ as determined from the refinements at 2 K.

The knowledge of the propagation vector $\mathbf{k} = (0,0,1.5)$ with the Ni²⁺-moments lying in the hexagonal ab -plane points towards two possible magnetic models for NiTiO₃: (a) FM layers stacked antiferromagnetically along the c -axis or (b) AFM layers with the spins aligned ferromagnetically along the c -axis. Previous static magnetic susceptibility $\chi = M/H$ vs. T measurements reveal the decrease of χ_{ab} below T_N whereas χ_c stays nearly constant^{22,26}. Moreover, the magnetic model (b) implies a zero magnetic structure factor at the position $Q = (0, 0, 1.5)$ contrary to our observation. Hence model (a) is most suitable to describe the magnetic structure of NiTiO₃. Hence, the obtained magnetic peaks at 2 K were refined against model (a) and a very good fit was obtained as shown in Fig. 4(b). The obtained magnetic structure of NiTiO₃ re-confirms the structure proposed by Shirane *et al.* based on powder neutron data as early as 1959¹⁴. The calculated intensities of several high-intensity peaks are listed in Table III and the complete magnetic structure of NiTiO₃ is schematically represented in Fig. 2(c). At $T = 2$ K, the ordered moment amounts to $1.46(1) \mu_B$.

The crystal symmetry of the basal hexagonal planes is marked by the presence of two sets of three two-fold axes. Hence, the rotated by 120° in-plane spin-configurations are exactly equivalent leading to the presence of spin domains (i.e., three domains). Since the refinements are usually performed using the average of the integrated intensities of the equivalent reflections, the directions of the spins cannot be uniquely determined using single-crystal neutron diffraction alone, similar to the problem existing in the powder diffraction experiments¹⁴. However, excellent agreement of the integrated intensities between the equivalent reflections ($R_{int} = 1.86\%$) indicates that there are likely three spin-domains of equal population with spins rotated by 120° in between the neighbouring domains.

C. Magneto-structural-dielectric coupling

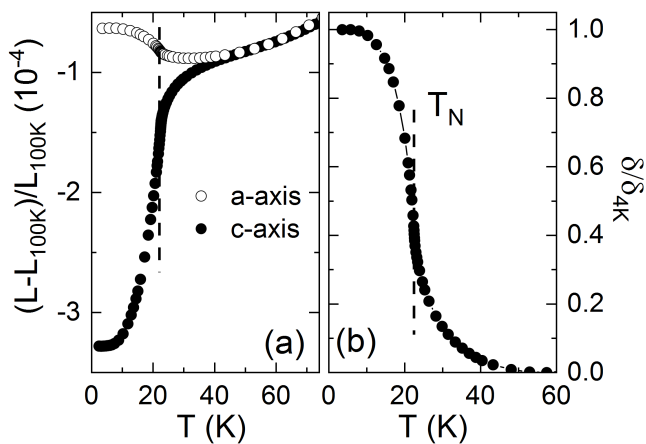


FIG. 3: (a) Relative length changes $dL_i^* = (L_i - L_i^{100K})/L_i^{100K}$ measured along the principle crystallographic a - and c -axis, respectively, by means of high-resolution dilatometry. (b) Normalised distortion parameter δ/δ_{4K} , with $\delta = (dL_a^* - dL_c^*)/(dL_a^* + dL_c^*)$. (c) Scaling of non-phononic linear thermal volume expansion volume (dV'/V) with the normalized dielectric permittivity digitized from ref²¹. The vertical dashed lines indicate T_N .

The magneto-structural coupling in NiTiO₃ has been studied by means of high-resolution capacitance dilatometry. The uniaxial relative length changes $dL_i^* = (L_i - L_i^{100K})/L_i^{100K}$ ($i = a, c$) (Fig. 3(a)) versus temperature show abrupt changes at T_N , i.e., shrinking of the c -axis and expansion along the a -axis, which demonstrates significant magnetoelastic coupling in NiTiO₃. At higher temperatures $T \geq 50$ K, isotropic thermal expansion coefficients results in similar rate of increase of dL_i^* along the a - and the c -axis, respectively. To further elucidate lattice changes at T_N , the normalized distortion parameter δ/δ_{4K} , with $\delta = (dL_a^* - dL_c^*)/(dL_a^* + dL_c^*)$, is shown in Fig. 3(b).

As evidenced by the distortion parameter, different behaviour of the a - and c -axis starts to evolve gradually below 50 K while δ sharply jumps at T_N (Fig. 3(a)). Evidently, onset of long-range AFM order is associated with a large spon-

aneous magnetostriction effect and it implies strong magneto-structural coupling. Large spontaneous magnetostriction has also been observed in other ilmenites such as FeTiO₃. The latter, however, shows a reversed magnetostrictive effect, i.e., there is an expansion of the c -axis and shrinking of the a -axis²⁰. We attribute this difference to the differing magnetic ground states in FeTiO₃ and NiTiO₃ and corresponding variation in magneto-crystalline anisotropy. Finite distortion δ up to 50 K evidences a precursor phase with short-range order well above T_N . Due to the observed strong magnetoelastic coupling we conclude the presence of short-ranged spin correlations persisting up to twice the transition temperature. This is corroborated by previous specific heat measurements²² on NiTiO₃ which reveal that nearly 20% of magnetic entropy is consumed between T_N and 50 K. In addition, it has been shown that \mathbf{q} -dependent spin-spin correlations couple to the dielectric response via the coupling of magnetic fluctuations to optical phonons, thereby causing a significant magnetocapacitive effect⁴⁶. Accordingly, we conclude the significant magnetocapacitance of 0.01% and finite magnetostriction recently observed in NiTiO₃ well above T_N is due to persisting spin-spin correlations^{21,22}.

D. Spin-reorientation

The effect of magnetic fields applied within the ab -plane on the crystal and magnetic structure of NiTiO₃ is studied by means of in-field neutron diffraction at 2 K. Specifically, the magnetic field is applied vertically along b -axis and the scattering vector lies in the $(H, 0, L)$ plane. Several nuclear and magnetic reflections were measured with rocking curve scans in magnetic-fields up to 6 T. As will be discussed below, there is a considerable decrease in intensity upon application of the magnetic field for all magnetic peaks while in contrast there is no magnetic field effect on the nuclear peak intensities. A representative scan through the magnetic peak $Q = (-1, 0, -2.5)$ is shown in the inset to Fig. 4.

The magnetization curve displays a non-linear dependence on magnetic fields applied along the ab -plane as evidenced by the magnetic susceptibility $\chi = \partial M/\partial B$ in Fig. 4(b). The maximum in χ at $B = 1.2$ T is indicative of a spin-reorientation transition. Correspondingly, the integrated magnetic intensity (Fig. 4(a)) shows a continuous decrease in magnetic fields up to 2 T above which it stays nearly constant at a finite value. Since the magnetic neutron diffraction intensity is proportional to the component of the magnetic moments perpendicular to the scattering vector, this observation indicates that in magnetic field the spins are rotated smoothly from three magnetic domains to a single domain state with spins are aligned perpendicular to fields above 2 T. Between 2 and 6 T, negligible field dependence indicates a very small canting of spins towards magnetic field. The FWHM calculated using Gaussian fits to nuclear peaks show negligible broadening up to 6 T indicating that the magnetostriction effects on lattice parameters corresponding to the spin-reorientation is below the experimental resolution.

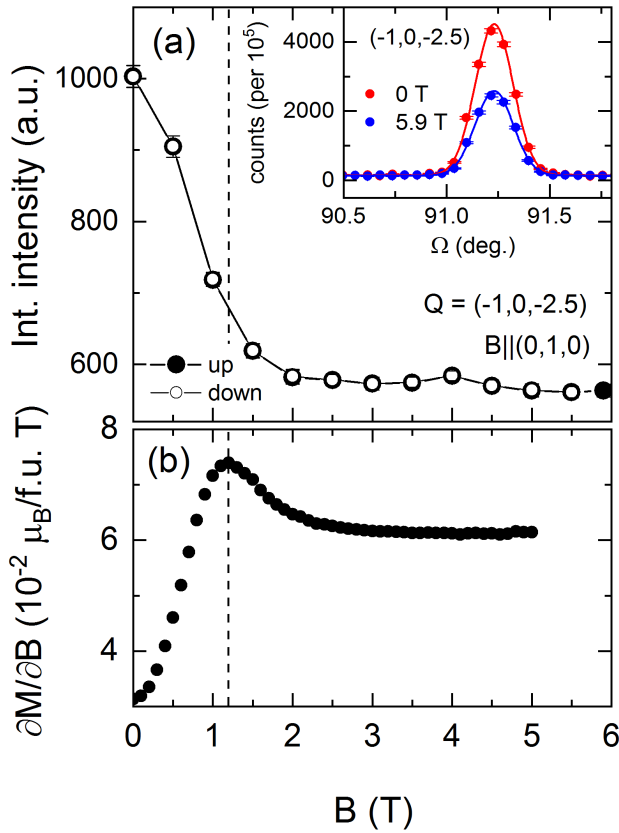


FIG. 4: (a) Integrated intensity of the magnetic $(-1,0,-2.5)$ peak as a function of magnetic field (up and down) and (b) the derivative of static magnetization with respect magnetic field $\partial M / \partial B$ as a function of magnetic field (from ref. 22) at 2 K. The inset to (a) shows the Ω -scans through the magnetic $(-1,0,-2.5)$ peak at 0 T and 5.9 T. The solid lines in blue and red are Gaussian fits to the peaks at 0 T and 5.9 T respectively.

E. Magnetostriction

Applying magnetic fields along the ab -plane yields a pronounced increase of the associated lattice parameter in the low-field region ($B < B^* = 2$ T) while there is only small magnetostriction at higher fields (see Fig. 5). Magnetostriction is also reportedly small for fields applied along c -axis²². We conclude that this behaviour is associated with the field-driven collective rotation of spins as discussed above and evidenced by Fig. 4. However, as will be discussed below, the magnetisation changes do not scale with magnetostriction and the maxima in $\partial M / \partial B$ and $\partial L_a / \partial B$ do not match each other (see Fig. 8(a)). The magnetostriction data hence do not correspond to what is expected for a thermodynamic spin-reorientation transition. Instead, the presence of domains has to be involved and in the following we will present clear evidence that the data represents the change from a low-field multi-domain state to a high-field uniform mono-domain one.

In order to further investigate the effect of in-plane magnetic fields, the intensity evolution of two equivalent magnetic Bragg peaks $(3,0,1.5)$ and $(-3,0,-1.5)$ belonging to two differ-

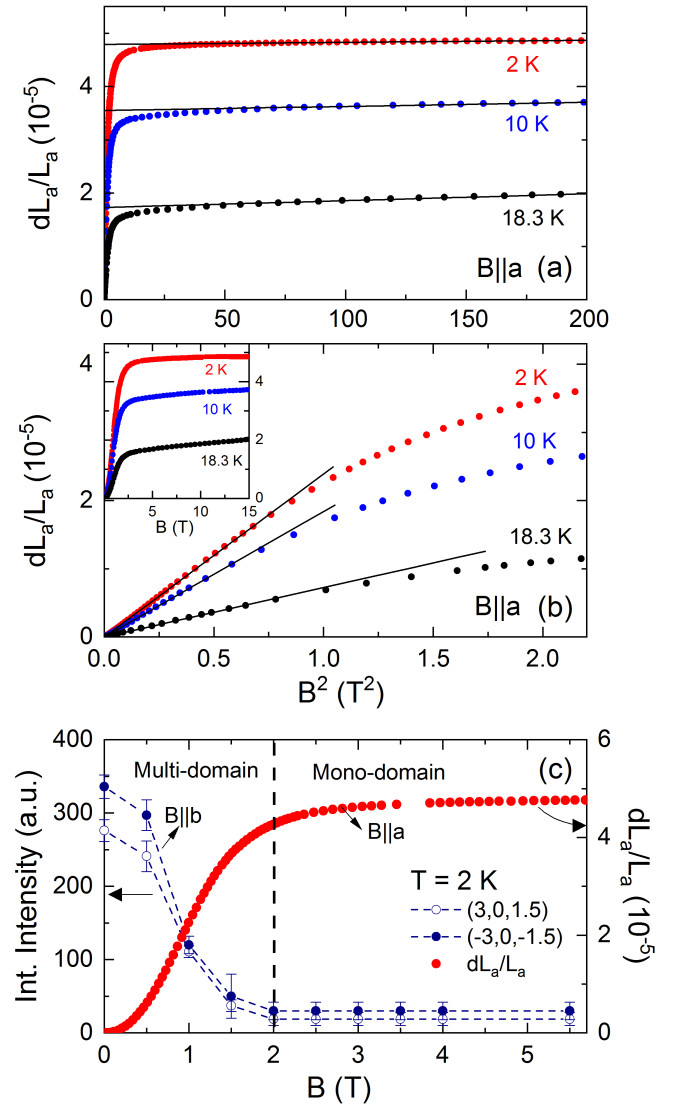


FIG. 5: Relative length changes dL_a / L_a , at different temperatures, versus the square of the magnetic field applied along the crystallographic a -axis for (a) magnetic fields up to 14 T, i.e., including the high-field single-domain (homogeneous) phase, and (b) for $B \leq 1.5$ T which is the low-field multi-domain phase (see the text). The solid black lines are corresponding linear fits. The inset to (b) shows the relative length changes versus applied magnetic field. (c) Integrated intensity of the equivalent magnetic Bragg peaks $(3,0,1.5)$ and $(-3,0,-1.5)$ vs. magnetic field applied along the b -axis and (dL_a / L_a) for fields along a -axis, at $T = 2$ K. The vertical dashed line separates the multi-domain and the mono-domain (homogeneous) regions. See text for more details.

ent magnetic domains is displayed in Fig. 5(c). In the multidomain state, the antiferromagnetic vector is uniform within a single domain and has different directions in different domains. The observed isotropic decrease in intensity of both magnetic peaks upon application of the magnetic field implies that the spins of both domains rotate perpendicularly to the external field direction. The spin-rotation process is completed at B^* which hence signals the formation of a spin-reoriented

monodomain state. Accordingly, no significant changes in the peak intensities are observed above B^* up to 6 T.

IV. DISCUSSION

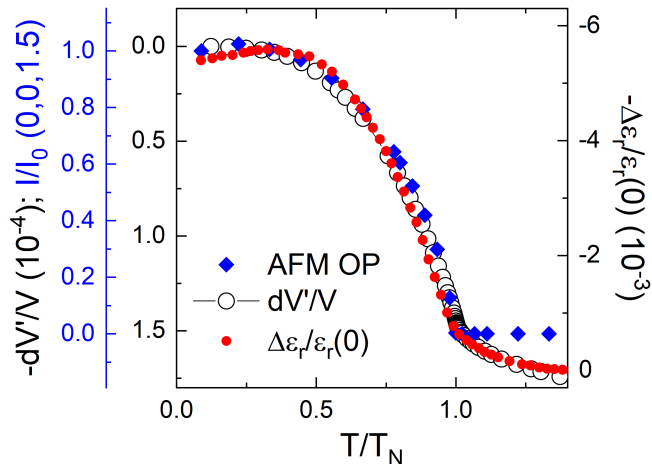


FIG. 6: Temperature dependence of the square of AFM order parameter, i.e., the normalised integrated intensity of the (0,0,1.5) magnetic Bragg peak, the negative non-phononic volume changes dV'/V , and the normalized dielectric permittivity digitized from Ref 21.

Comparison of the magnetic order parameter and the relative volume changes with the reported data of the dielectric function by Harada *et al.*²¹ elucidates the coupling mechanism between the lattice and the dielectric degrees of freedom in NiTiO₃. As displayed in Fig. 6(a), the non-phononic relative volume changes $dV'/V = 2(dL_a/L_a) + (dL_c/L_c)$ which are obtained by subtracting the phononic contribution from dV/V (cf. Ref. 22) show a very similar temperature dependence, below T_N , as the normalized dielectric permittivity. Note, that the polycrystalline sample studied in Ref. 21 displays a slightly lower T_N than the single crystals studied at hand. Note, that in general length changes can directly affect the experimentally measured permittivity via the relation $\epsilon = Cd/\epsilon_0 A$, where C , ϵ_0 , d and A are sample capacitance, vacuum permittivity, sample thickness and area, respectively. However, the changes in sample dimensions at T_N are on the order of 10^{-4} , while the relative change in permittivity an order higher, implying that spontaneous magnetostriction is not the driving mechanism for the observed dielectric changes at T_N . Interestingly, the normalized dielectric permittivity varies as square of the antiferromagnetic order parameter ' L ' represented by the normalized integrated intensity of the magnetic (0,0,1.5) Bragg peak in Fig. 6(a). In order to discuss this, we recall the Landau expansion of the free energy F , in terms of polarization P , and the sub-lattice magnetization L at zero magnetic-field⁴⁷:

$$F = F_0 + \alpha P^2 + \alpha' L^2 + \beta PL + \gamma P^2 L^2 - PE \quad (1)$$

The dielectric function is obtained as $\partial^2 F / \partial P^2 = \epsilon \propto$

γL^2 . Hence Fig. 6(a) qualitatively evidences the presence of magnetodielectric coupling in NiTiO₃. On top of the spin and dielectric changes, the structural changes exhibits similar behaviour below T_N . Previously reported magnetic Grüneisen analysis²² evidences that the entropic changes at T_N to be of purely magnetic nature. In our opinion the spin-phonon coupling is responsible for observed dielectric changes at T_N . In the presence of spin-phonon coupling the phonon frequency ω can be affected by spin-correlation as $\omega = \omega_0 + \lambda \langle S_i \cdot S_j \rangle$ resulting in modification of permittivity via the Lyddane-Sachs-Teller equation $\epsilon_0 = \omega_L^2 / \omega_T^2 \epsilon_\infty$, where ϵ_0 and ϵ_∞ are the permittivity at zero frequency and optical frequency, respectively and ω_L^2 and ω_T^2 are the long-wavelength longitudinal and transverse optical phonon modes respectively.

It is noteworthy that apart from spontaneous magnetostriction, an exchange-striction (ES) mechanism may in principle also lead to spontaneous lattice deformation at T_N and be a potential source for dielectric anomaly at T_N . Magnetodielectricity fueled by ES mechanism have been observed in several systems for example Y₂Cu₂O₅⁴⁸ and TeCuO₃⁴⁶. In FeTiO₃ a combination of ES and magnetostriction mechanisms have been suggested for the spontaneous lattice deformation at T_N ²⁰. In particular for NiTiO₃ an ES mechanism would imply a change in Ni-O-Ni bond angle in the ab plane closer to 90° favouring ferromagnetic super-exchange. However, diffraction experiments reveal that the bond angle increases from 90.34° at 100 K to 90.36° at 2 K (supplementary Fig. 2), contrary to predictions of ES. Hence, ES mechanism is excluded as the origin of lattice distortion at T_N in NiTiO₃.

The crystallographic symmetry of the easy hexagonal plane in NiTiO₃ suggests the presence of three domains with spins rotated by 120° in different domains. Such a spin structure with three domains is often observed in easy-plane-type hexagonal antiferromagnets such as CoCl₂, NiCl₂, and BaNi₂V₂O₈^{49,50}. In NiTiO₃, the magnetostriction data imply that the field-driven changes of the domain structure is associated with structural changes. Indeed, orientational AFM domains are magnetoelastic in nature^{51,52} and have previously been observed in various systems, for example in cubic antiferromagnets RbMnF₃⁵³, KNiF₃ and KCoF₃^{54,55}, NiO⁵⁶, iron-group dihalides CoCl₂⁵⁷ and NiCl₂⁵⁸, the quasi-two-dimensional AFM BaNi₂V₂O₈⁵⁰, YBa₂Cu₃O_{6.3}⁵² etc. In particular, Kalita and co-workers have developed phenomenological theories describing the effect of domain re-distribution on the magnetostriction for CoCl₂ and NiCl₂⁵⁷⁻⁶¹. Note, that both NiCl₂ and CoCl₂ are easy-plane-type antiferromagnets with similar crystalline symmetry, i.e., trigonally distorted octahedral environment surrounding metal ions, similar to NiTiO₃ and CoTiO₃^{49,62}. In the following, we will describe the field-dependency of the lengths changes in NiTiO₃ based on the phenomenological theories developed by Kalita and co-workers.

Both at low magnetic fields $B||a \leq 1$ T and at high fields the field-induced striction dL_a/L_a varies as the square of the applied magnetic field as shown in Fig. 5(a,b). In the latter, i.e., the mono-domain state, this is predicted by calculating the equilibrium elastic strain by energy minimization of the magnetoelastic and the elastic contributions to the free energy^{57,58}.

The magnetostriction in the mono-domain state is described by

$$(dL_a/L_a)(T, B) = \alpha(T)(B)^2 + (dL_a/L_a)_s(T, B = 0 \text{ T}) \quad (2)$$

where $\alpha(T)$ is the temperature dependent slope and $(dL_a/L_a)_s(T, H = 0)$ is the spontaneous magnetostriction of the mono-domain state obtained by extrapolating the linear fit to $B = 0$ T. Eq. 2 fits well with dL_a/L_a at different temperatures as shown by the solid black lines in Fig. 5(a). The obtained fit parameters are listed in Table IV. $(dL_a/L_a)_s$ corresponds to a hypothetical spontaneous striction that would be observed if the magnetoelastic domains did not appear at low fields, i.e., if the total spontaneous magnetostriction was not compensated on the whole by summation of strains in different directions in each of the domains.

The magnetostrictive response upon application of magnetic fields in the multi-domain state is governed by domain-wall motion. Specifically, magnetostriction is large due to the associated facilitated rotation of spins. The motion of magnetoelastic domain-walls is predominantly reversible in nature^{51,54} and the associated lengths changes again exhibit a square-dependence on the magnetic field which is expressed by

$$(dL_a/L_a)(T, H) = (dL_a/L_a)_s(T, H = 0)(H/H_d)^2. \quad (3)$$

Here, H_d is an empirical parameter obtained from the fits (see Table IV). As shown in Fig. 5(b), the experimental data are well described by Eq. 3 which is in-line with the predictions of phenomenological models^{54,58}. Although the magnetoelastic domains are predominately reversible in nature, a small irreversibility may arise due to pinning of domain walls by crystal defects and imperfections in the crystals. A small remanent striction amounting to $\sim 1.6 \times 10^{-6}$, at $T = 2$ K, is indeed observed in our data (see the Supplement Fig. 1) which indicates the presence of predominately mobile domain walls⁵¹ in NiTiO₃.

TABLE IV: Parameters obtained from fits to the magnetostriction data (Fig. 5(a,b)) using Eqs. 2 and 3. $(dL_a/L_a)_s$ is the spontaneous magnetostriction (see the text).

T	$(dL_a/L_a)_s(10^{-5})$	H_d (T)	$\alpha(10^{-9})(\text{T}^2)$
2 K	4.79	1.41	3.8
10 K	3.55	1.38	7.6
18.3 K	1.73	1.55	12.8

Unlike uniaxial antiferromagnets which show an abrupt magnetization jump at the spin-flop transition as, e.g., observed in MnTiO₃⁶³, the magnetization in NiTiO₃ follows a sickle-shaped field dependence in the non-flopped phase and the reorientation transition is associated with smooth right bending in M vs. B (see Fig. 7). Such characteristic smooth non-linear variation of magnetization in low-fields is a manifestation of the multi-domain state where spin-reorientation

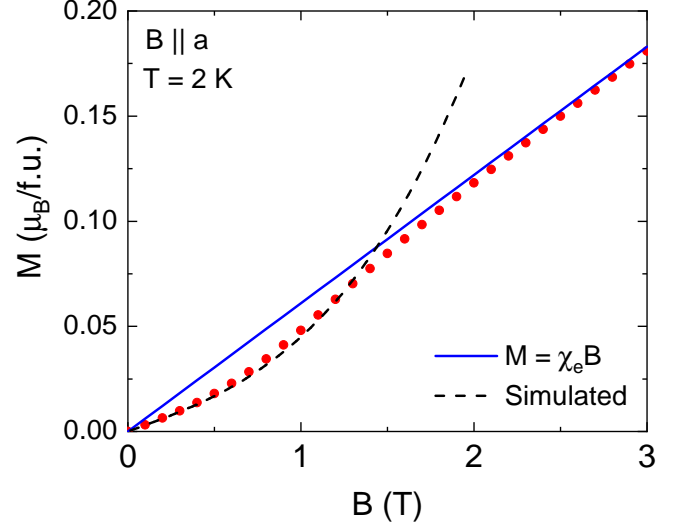


FIG. 7: Magnetization M , at $T = 2$ K, versus applied magnetic field $B||a$ -axis. The solid blue line represents a linear fit to M in the high-field region and the dashed black line shows a simulation to M at low fields (see the text for more details).

takes place gradually by displacement of domain walls⁵⁵. This is described⁶¹ by

$$M = (1/2)\chi_e B[1 + (B/B_d)^2] \quad (4)$$

where χ_e is the high-field magnetic susceptibility. A linear fit to the M vs. B curve²² at $B > 4$ T yields $\chi_e = 0.06 \mu_B/\text{f.u.}\cdot\text{T}$ which is represented by the solid blue line in Fig. 7. Using H_d from the analysis of the magnetostriction data (see Table IV) enables to deduce the field dependence of M . The simulation using Eq. 4 is shown by the dashed line in Fig. 7. It yields a good description of the field-driven evolution of the magnetization in the multi-domain state, thereby further confirming the applied phenomenological model. The blue line in Fig. 7 represents the expected magnetization in a single-domain easy-plane AFM with no in-plane anisotropy.

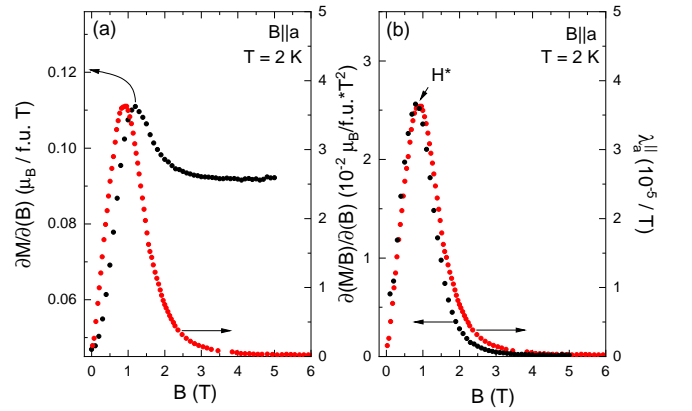


FIG. 8: (a) Scaling of $\partial M / \partial B$, (b) $\partial(M/B) / \partial B$ and λ_a^{\parallel} versus B at $T = 2$ K.

The field-driven disappearance of the multi-domain state yields different behaviour of the magnetic susceptibility $\partial M/\partial B$ and the magnetostriction $\partial L/\partial B$. This is demonstrated in Fig. 8(a) where the derivative of the magnetization and the longitudinal magnetostriction coefficient $\lambda_a^{\parallel} = (1/L_a)\partial L_a/\partial(\mu_0 H)$ are shown at $T = 2$ K as a function of B . The data are scaled to match the corresponding peak values. According to the Ehrenfest relation

$$\partial B^*/\partial p_i = V_m \Delta \lambda_i / \Delta[\partial M/\partial(\mu_0 H)] \quad (5)$$

Using molar volume $V_m = 42.01$ cm³/mol and $B^* = 0.8$ T (Fig. 8(b)), we obtain the normalized pressure dependency $(1/B^*)\partial B^*/\partial p = 0.8$ kbar⁻¹. Positive magnetostriction in the mono-domain phase reveals that (see also Fig. 5 (a)) for each domain the in-plane distortion in magnetic field is such that the lattice expands perpendicular to the spin-direction. Hence, applying a uniaxial pressure p will induce an anisotropy in plane favouring domains with spins nearly parallel to p in the multi-domain phase.

The scaling of $\partial(M/H)/\partial(\mu_0 H)$ and λ_a^{\parallel} at 2 K in Fig. 8(b) shows that the quantities vary proportional to each other in the multi-domain state peaking at B^* . The proportional variation $d(m/H)/dH \sim \lambda_a^{\parallel}$ is consistent with equation 3 and is manifestation of magnetoelastic nature of the domains. The behaviour is expected from phenomenological theories of magnetoelastic domains which describe the variation of magnetization and length changes by means of a single domain co-alignment parameter and its variation with magnetic field⁶⁰.

Apart for large magneto-crystalline anisotropy which dictates the easy-plane spin structure in NiTiO₃, an additional small in-plane anisotropy may arise due to frozen strains in the domain walls^{64,65}. Small in-plane anisotropy has been previously observed in other easy-plane type antiferromagnets like the dihalides NiCl₂ (~ 0.3 T) and CoCl₂ (~ 0.8 T) by means of low-frequency resonance experiments⁶⁴ and in CoTiO₃ (~ 1 meV) by means of INS experiments²⁵ respectively. Although bond anisotropic exchange interaction pinning the order pa-

rameters to the crystal axes²⁴ was suggested as the responsible mechanism for small in-plane gap in CoTiO₃ we believe that a small in-plane anisotropy to be present in NiTiO₃ corresponding to magnetoelastic domain walls.

V. SUMMARY

In summary, we have studied in detail the magnetostructural coupling in magnetodielectric NiTiO₃ by means of single crystal neutron-diffraction and high-resolution dilatometry. Zero-field neutron diffraction reveals multidomain A-type spin antiferromagnetic ordering with preservation of crystallographic $R\bar{3}$ symmetry down to 2 K. Zero-field thermal expansion measurements reveals spontaneous lattice deformation at T_N . The dielectric permittivity ϵ scales with the square of magnetic order parameter L in line with predictions of Landau theory and hence indicating finite magnetodielectric coupling in NiTiO₃. Our analysis suggests the presence of spin-phonon coupling as a responsible mechanism for dielectric anomaly at T_N in NiTiO₃. In-field neutron diffraction shows the evolution of magnetic domains with spins perpendicular to the applied field. The effect of magnetic domains on magnetostriction have been discussed in light of phenomenological multi-domain theories. We see magnetization and magnetostriction scale with each other in the multidomain state revealing strong coupling of spins to the lattice.

Acknowledgments

This work has been performed in the frame of the International Max-Planck School IMPRS-QD. We acknowledge support by BMBF via the project SpinFun (13XP5088) and by Deutsche Forschungsgemeinschaft (DFG) under Germany's Excellence Strategy EXC2181/1-390900948 (the Heidelberg STRUCTURES Excellence Cluster) and through project KL 1824/13-1.

* email:kaustav.dey@kip.uni-heidelberg.de

¹ R. Zhong, T. Gao, N. P. Ong, and R. J. Cava, *Sci. Adv.* **6** (2020).

² H. Liu and G. Khaliullin, *Phys. Rev. B* **97**, 014407 (2018).

³ S. S. Pershoguba, S. Banerjee, J. C. Lashley, J. Park, H. Ågren, G. Aeppli, and A. V. Balatsky, *Phys. Rev. X* **8**, 011010 (2018).

⁴ L. Chen, J.-H. Chung, B. Gao, T. Chen, M. B. Stone, A. I. Kolesnikov, Q. Huang, and P. Dai, *Phys. Rev. X* **8**, 041028 (2018).

⁵ T. Matsumoto and S. Hayami, *Phys. Rev. B* **101**, 224419 (2020).

⁶ A. I. Kurbakov, A. N. Korshunov, S. Y. Podcherezstev, A. L. Malyshev, M. A. Evstigneeva, F. Damay, J. Park, C. Koo, R. Klingeler, E. A. Zvereva, et al., *Phys. Rev. B* **96**, 024417 (2017).

⁷ A. Nakua and J. Greedan, *J. Solid State Chem.* **118**, 402 (1995).

⁸ C. Koo, E. A. Zvereva, I. L. Shukaev, M. Richter, M. I. Stratan, A. N. Vasiliev, V. B. Nalbandyan, and R. Klingeler, *J. Phys. Soc. Japan* **85**, 084702 (2016).

⁹ K. S. Burch, D. Mandrus, and J.-G. Park, *Nature* **563**, 47 (2018).

¹⁰ A. Maignan and C. Martin, *Phys. Rev. Materials* **2**, 091401(R) (2018).

¹¹ J. Werner, W. Hergett, M. Gertig, J. Park, C. Koo, and R. Klingeler, *Phys. Rev. B* **95**, 214414 (2017).

¹² N. D. Khanh, N. Abe, K. Matsuura, H. Sagayama, Y. Tokunaga, and T. Arima, *Appl. Phys. L* **114**, 102905 (2019).

¹³ J. B. Goodenough and J. J. Stickler, *Phys. Rev.* **164**, 768 (1967).

¹⁴ G. Shirane, S. Pickart, and Y. Ishikawa, *J. Phys. Soc. Japan* **14**, 1352 (1959).

¹⁵ R. E. Newnham, J. H. Fang, and R. P. Santoro, *Acta Crystallographica* **17**, 240 (1964).

¹⁶ J. J. Stickler, S. Kern, A. Wold, and G. S. Heller, *Phys. Rev.* **164**, 765 (1967).

¹⁷ G. S. Heller, J. J. Stickler, S. Kern, and A. Wold, *J. Applied Phys.* **34**, 1033 (1963).

¹⁸ J. Akimitsu, Y. Ishikawa, and Y. Endoh, *Solid State Comm.* **8**, 87

- (1970).
- ¹⁹ N. Mufti, G. R. Blake, M. Mostovoy, S. Riyadi, A. A. Nugroho, and T. T. M. Palstra, *Phys. Rev. B* **83**, 104416 (2011).
 - ²⁰ M. Charilaou, D. Sheptyakov, J. F. Löffler, and A. U. Gehring, *Phys. Rev. B* **86**, 024439 (2012).
 - ²¹ J. K. Harada, L. Balhorn, J. Hazi, M. C. Kemei, and R. Seshadri, *Phys. Rev. B* **93**, 104404 (2016).
 - ²² K. Dey, S. Sauerland, J. Werner, Y. Skourski, M. Abdel-Hafiez, R. Bag, S. Singh, and R. Klingeler, *Phys. Rev. B* **101**, 195122 (2020).
 - ²³ R. M. Dubrovin, N. V. Siverin, M. A. Prosnikov, V. A. Chernyshev, N. N. Novikova, P. C. M. Christianen, A. M. Balbashov, and R. Pisarev, *J. Alloys and Compounds* p. 157633 (2020).
 - ²⁴ B. Yuan, I. Khait, G.-J. Shu, F. C. Chou, M. B. Stone, J. P. Clancy, A. Paramekanti, and Y.-J. Kim, *Phys. Rev. X* **10**, 011062 (2020).
 - ²⁵ M. Elliot, P. A. McClarty, D. Prabhakaran, R. D. Johnson, H. C. Walker, P. Manuel, and R. Coldea (2020), arXiv:2007.04199.
 - ²⁶ H. Watanabe, H. Yamauchi, and H. Takei, *J. Magn. Magnetic Mat.* **15-18**, 549 (1980).
 - ²⁷ R. KÜchler, T. Bauer, M. Brando, and F. Steglich, *Rev. of Sci. Instruments* **83**, 095102 (2012).
 - ²⁸ T. Barth and E. Posnjak, *Zeit für Krist.* p. 271 (1934).
 - ²⁹ K. Kabsch, *International Tables for Crystallography*, vol. F (Kluwer Academic Publishers, Dordrecht, 2001).
 - ³⁰ *CrysAlisPro*, Agilent Technologies UK Ltd., Oxford (2011).
 - ³¹ R. H. Blessing, *Acta Cryst.* **A51** (1995).
 - ³² *SCALE3 ABSPACK*, *CrysAlisPro*, Agilent Technologies UK Ltd., Oxford (2011).
 - ³³ W. R. Busing and A. Levy, *Acta Cryst.* **10** (1957).
 - ³⁴ *SHELXT*, University of Göttingen and Bruker AXS GmbH, Karlsruhe, Germany (2012-2018).
 - ³⁵ M. Ruf, B. C. Noll, *Application note SC-XRD 503*, Bruker AXS GmbH, Karlsruhe, Germany (2014).
 - ³⁶ G. sheldrick, *Acta Cryst.* **A71** (2015).
 - ³⁷ *SHELXL-20xx*, University of Göttingen and Bruker AXS GmbH, Karlsruhe, Germany (2012-2018).
 - ³⁸ W. Robinson and G. M. Sheldrick, *Crystallographic Computing 4* (IUCr and Oxford University Press, Oxford, UK, 1988).
 - ³⁹ G. sheldrick, *Acta Cryst.* **A64** (2008).
 - ⁴⁰ G. sheldrick, *Acta Cryst.* **C71** (2015).
 - ⁴¹ P. J. Brown, A. G. Fox, H. H.-C., J. I. Langford, H. Lipson, E. N. Maslen, M. A. O'Keefe, T. M. Sabine, and B. T. M. Willis, *International Tables for Crystallography*, vol. C (Kluwer Academic Publishers, Dordrecht, The Netherlands., 2004), 3rd ed.
 - ⁴² P. Azavant and A. Lichanot, *Acta Cryst.* **A49** (1993).
 - ⁴³ Morelhão, *Computer simulation tools for X-ray analysis* (Springer International Publishing Cham, Switzerland, 2016), 3rd ed., URL <http://http://xraybook.if.usp.br>.
 - ⁴⁴ A. C. Larson, *Crystallographic computing* (Munksgaard, Copenhagen, Denmark, 1970).
 - ⁴⁵ CSD 2062660 (model A), 2062661 (model B) and 2062662 (model C) contains the supplementary crystallographic data for this paper. These data can be obtained from the Cambridge Crystallographic Data Centre's and FIZ Karlsruhe's joint Access Service via <https://www.ccdc.cam.ac.uk/structures/>
 - ⁴⁶ G. Lawes, A. P. Ramirez, C. M. Varma, and M. A. Subramanian, *Phys. Rev. Lett.* **91**, 257208 (2003).
 - ⁴⁷ T. D. Sparks, M. C. Kemei, P. T. Barton, R. Seshadri, E.-D. Mun, and V. S. Zapf, *Phys. Rev. B* **89**, 024405 (2014).
 - ⁴⁸ U. Adem, G. Nénert, Arramel, N. Mufti, G. R. Blake, and T. T. M. Palstra, *Eur. Phys. J. B* **71**, 393 (2009).
 - ⁴⁹ M. K. Wilkinson, J. W. Cable, E. O. Wollan, and W. C. Koehler, *Phys. Rev.* **113**, 497 (1959).
 - ⁵⁰ W. Knafo, C. Meingast, K. Grube, S. Drobnik, P. Popovich, P. Schweiss, P. Adelman, T. Wolf, and H. v. Löhneysen, *Phys. Rev. Lett.* **99**, 137206 (2007).
 - ⁵¹ E. V. Gomonaj and V. M. Loktev, *Low Temp. Phys.* **25**, 520 (1999).
 - ⁵² H. Gomonay and V. M. Loktev, *J. Phys.: Cond. Matter* **14**, 3959 (2002).
 - ⁵³ Y. Shapira and N. F. Oliveira, *Phys. Rev. B* **18**, 1425 (1978).
 - ⁵⁴ M. Safa and B. Tanner, *Phil. Mag. B* **37**, 739 (1978).
 - ⁵⁵ B. Tanner, *Contemporary Phys.* **20**, 187 (1979).
 - ⁵⁶ T. Yamada, S. Saito, and Y. Shimomura, *J. Phys. Soc. of Japan* **21**, 672 (1966).
 - ⁵⁷ V. M. Kalita, A. F. Lozenko, and S. M. Ryabchenko, *Low Temp. Phys.* **26**, 489 (2000).
 - ⁵⁸ V. M. Kalita, A. F. Lozenko, and P. A. Trotsenko, *Low Temp. Phys.* **28**, 263 (2002).
 - ⁵⁹ V. M. Kalita and A. F. Lozenko, *Low Temp. Phys.* **27**, 645 (2001).
 - ⁶⁰ V. M. Kalita, A. F. Lozenko, P. A. Trotsenko, and T. M. Yatkevich, *Low Temp. Phys.* **30**, 27 (2004).
 - ⁶¹ V. M. Kalita, A. F. Lozenko, S. M. Ryabchenko, and P. A. Trotsenko, *Low Temp. Phys.* **31**, 794 (2005).
 - ⁶² M. E. Lines, *Phys. Rev.* **131**, 546 (1963).
 - ⁶³ H. Yamaguchi, H. Hiroyoshi, M. Yamada, H. Watanabe, and H. Takei, *J. Mag. Magnetic Mat.* **31-34**, 1071 (1983).
 - ⁶⁴ A. F. Lozenko and S. M. Ryabchenko, *Soviet J. Exp. Theo. Phys.* **38**, 538 (1974).
 - ⁶⁵ N. B. Weber, H. Ohldag, H. Gomonaj, and F. U. Hillebrecht, *Phys. Rev. Lett.* **91**, 237205 (2003).